Controllable Substitution of S Radicals on Triazine Covalent Framework to Expedite Degradation of Polysulfides

Yingchun Yan, Zhou Chen, Jun Yang, Lu Guan, Han Hu, Qingshan Zhao, Hao Ren, Yan Lin, Zhongtao Li,* and Mingbo Wu*

Lithium–sulfur (Li–S) batteries are facing a significant barrier due to the diffusion of intermediate redox species. Although some S doped covalent framework cathodes have been reported with outstanding reversibility, the low content of sulfur (less than 30%) limits the practical applications. To overcome the issue, the sulfur and nitrogen co-doped covalent compounds (S-NC) as a host-type cathode have been developed through the radical transfer process during thermal cracking amino groups on the precursor, and then plentiful positively charged sulfur radicals can be controllably introduced. The experimental characterization and DFT theoretical calculation certificate that the sulfur radicals in S-NC/S can expedite redox reactions of intermediate polysulfides to impede their dissolution. Moreover, the energy barriers during ions transfer also obviously decreased after introducing S radicals, which lead to improved rate performance.

1. Introduction

To overcome the insulating nature, the notorious shuttling effect, and the large volumetric change of elemental sulfur in Li–S cathode during lithiation/delithiation, many strategies have been developed, including encapsulating sulfur into an electrically conductive carbon such as graphene/graphene oxide.[1] However, due to the weak physical interaction between carbon matrix and polysulfides, they still cannot serve as the perfect host-type cathode to overcome capacity degradation during cycling. One effective protocol to enhance interaction with polysulfides is the introduction of heterocycle into conjugated carbon matrix to increase the interaction of polysulfides with substrates.[2] Moreover, this strategy could avoid more expensive heavy metals and complicated protocol on nanostructure modulation, which could benefit scale-up manufacturing and lower cost, while the insight of hetero-doped carbonic electrode stabilizing polysulfides is still not well understudied.

Generally, increasing the content of heteroatom in the carbon matrix could attribute more active sites to coordinate

sulfur, which needs lower carbonization temperature to avoid deep thermal cracking. Therefore, the development of highly conductive hybrid carbon cathode with a more active surface still meets a great challenge. Covalent organic frameworks with N-doped subunits (COFs) with high porosity have attracted increasing concerns,[3] among which some S doped NCOFs have been reported with high charge transfer mobility.[4] Co-annealing S with PAN could effectively introduce massive S—S bonds onto cathode materials, which could reversibly convert to S radicals to coordinate Li during cycling.[5] However, the low content of sulfur (less than 30%) decreased over-all mass-energy density and limited the practical application further. So it is meaningful to adopt S doped NCOFs in the host-type cathode and understand the effect of doped S and their synergistic effect with N on restricting polysulfides.

Although the generation of S—S bonds in S doped carbon materials has been proved in previous reports, the formation mechanism and modulation protocol have not been well studied. In general, the substitution of sulfur on molecules should be through a radical process or nucleophilic reaction. Therefore, the introduction of some active sites during thermal doping or co-doping in an alkaline atmosphere would accelerate the procedure of sulfur doping. Herein, diaminomaleonitrile (DAMN) was adopted as a precursor and thermal doped in melted sulfur in a sealed kettle. The nitrogen-doped covalent compound (NC) could start to be generated through the polymerization of cyano groups at 300 °C. Moreover, the amino-groups on DAMN were thermal cracked over 370 °C, which converted to abundant radicals and alkaline ammonia. In this regard, most S radicals substituted on the neighbor of C=N in the carbon matrix and stimulated to achieve more electrochemical active doping subunits at elevated temperatures. The experiment data revealed that the sulfur and nitrogen co-doped covalent compounds (S-NC) can effectively stabilize stored sulfur and accelerate the kinetics of lithium polysulfides (LiPSs) conversion at the cathode, which leads to improved Li–S batteries' performance.

2. Results and Discussion

As illustrated in **Scheme 1**, S-NC has been synthesized by thermal polymerization of DAMN in melted sulfur at 400 °C

Y. Yan, Z. Chen, J. Yang, L. Guan, Prof. H. Hu, Dr. Q. Zhao, Dr. H. Ren, Dr. Y. Lin, Prof. Z. Li, Prof. M. Wu
State Key Laboratory of Heavy Oil Processing
College of Chemical Engineering
China University of Petroleum (East China)
Qingdao 266580, P. R. China
E-mail: liztao@upc.edu.cn; wumb@upc.edu.cn

The ORCID identification number(s) for the author(s) of this article can be found under https://doi.org/10.1002/smll.202004631.
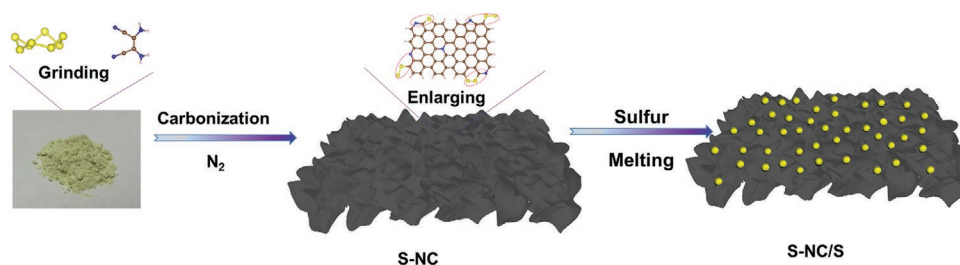
Scheme 1. The synthetic protocol of S-NC and S-NC/S.

for 12 h with nitrogen protection, and then soxhlet extracted for 24 h by toluene to dissolve excess sulfur. As a control sample, NC was synthesized via the same method without the addition of sulfur during thermal polymerization. In the spectra of Fourier transform infrared (FT-IR) in **Figure 1**a, the absorption peak from stretching C≡N bands at 2218 cm^{-1} vanished in the profile of S-NC and the new characteristic absorption bands appeared at 1500–1700 cm^{-1}, all of which proved the conversion from C≡N bands to triazine rings through trimerization.[6] Moreover, the stretching absorption at 751 and 550–600 cm^{-1} represented the formation of C—S and S—S bond after S doping,[7] respectively. Without the introduction of sulfur during polymerization, the absorption peaks of C≡N in the profile of DAMN also disappeared and new characteristic absorption bands of triazine rings increased in the profile of NC during polymerization. In the Raman spectra, the slight red shift of D and G

bands in S-NC than that in NC (Figure S1, Supporting Information) would be attributed to the weakening C—C bonds by the electrical withdrawing effect of doped sulfur. Moreover, 454 and 543 cm^{-1} of S—S bonds and the peaks at 804 cm^{-1} of C—S bonds indicated two types of doped S.[8] The pore size distribution of S-NC and NC is shown in Figure S2, Supporting Information. S-NC exhibits more diverse pore structures than NC, which can effectively improve sulfur utilization and battery cycle performance.[9] In Figure S3, Supporting Information, the morphology of S-NC and NC were characterized by scanning electron microscopy (SEM), both of which show porous structures. The energy dispersive X-ray (EDX) mapping image of S-NC reveals that carbon, nitrogen, sulfur are homogenously distributed (Figure S4, Supporting Information).

In the ^{13}C spectra of S-NC (Figure 1b), the peak of sp^2 hybrid carbon in C=N (154 ppm) moves to a low field after S doping
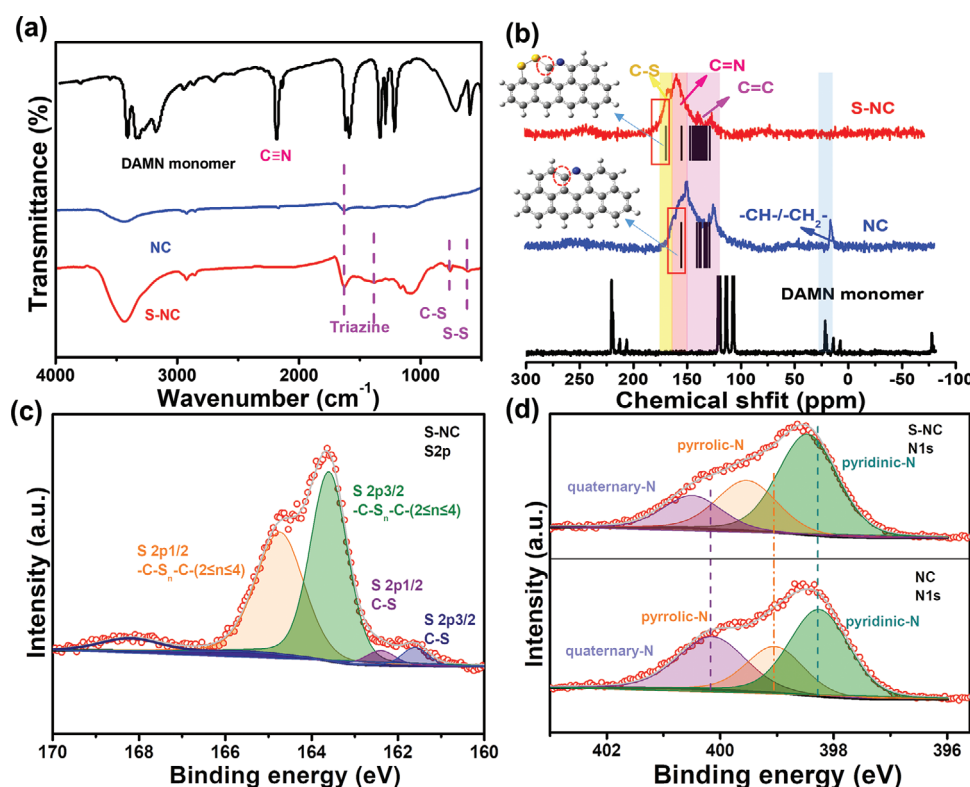

Figure 1. a) FT-IR spectra of DAMN monomer, NC, and S-NC. b) The experimental data of ^{13}C MAS solid-state NMR spectra of DAMN monomer, NC, and S-NC. The inside is the calculated ^{13}C NMR spectra of atoms between S-NC and NC structure. The simulation locations of C are in the o-position of nitrogen atom (Note: the yellow, blue, gray, and white cross point represent S, N, C, and H atoms. The position of carbon was indicated with a red circle.) c) High-resolution S2p XPS spectra of S-NC. d) High-resolution N1s XPS spectra of S-NC and NC.

**ADVANCED
SCIENCE NEWS**
www.advancedsciencenews.com

NANO · MICRO
small
www.small-journal.com

(149 ppm in NC), which indicated the introduced S should substitute on the carbon neighbor of C=N.[10] The result was further proven in the calculations. We discuss three substitution positions of the carbon (Figure 1b and Figure S5, Supporting Information) and find that the simulations of ^{13}C NMR shift most pronounced when the substitution is in the o-position of C=N. While, the shift of C=C peaks at 120–136 ppm in S-NC than that in NC, which is attributed to the introduction of S. Moreover, the signal in NC at 13.6 ppm corresponds to sp^3 hybrid carbon of –CH–/–CH$_2$–, which indicates the incomplete conversion of the –CN during polymerization without S. The X-ray photoelectron spectroscopy (XPS) spectra of S-NC and NC are displayed in Figures S6 and S7, Supporting Information, 1c and 1d. The C1s spectra of S-NC and NC (Figure S7, Supporting Information) exhibited four peaks located at 284.6, 285.5, 286.4, and 287.5 eV, corresponding to C−C(C=C), C−S, C−N, and N=C−N, respectively. In contrast, there is no C−S band and the peak of N=C-N is weak in the C1s spectrum of NC. The results further uncover the formation of covalent C−S bonds present and the existence of sulfur catalyst contributes to form a conjugated organic framework. The high-resolution S 2p XPS spectrum in Figure 1c displayed three major peaks with binding energies of 163.6, 164.7, 162.4, and 161.6 eV, corresponding to S 2p3/2, S 2p1/2 states of the C−S$_n$−C ($2\leq n \leq 4$) and single C−S bonds,[8a,11] respectively. The XPS N1s core-level spectrum of S-NC and NC (Figure 1d) perfectly shows the nitrogen content distribution. The consistency with the EA (elemental analysis) characterization data indicated the homogenous dispersion of N and universal structure throughout S-NC and NC (Table S1, Supporting Information). Besides, the pyridinic-N (17.5 at%)

and pyrrolic-N (8.80 at%) in S-NC, are higher than that in NC (Table S2 and Figure S8, Supporting Information), which indicates that sulfur doping contributes to the formation of higher pyridinic-N and pyrrolic-N. The binding affinity with LiPSs can be greatly improved by pyridinic-N and pyrrolic-N, which would give rise to reversible capacity.[12]

To further understand the state of doped S, **Figure 2**a displays the electron paramagnetic resonance (EPR) spectra of five samples, all of which show a similar signal at g = 2.00, which is ascribed to S radicals.[13] The signal of S radicals in sublimed S and NC is hard to be identified. Some S radicals could be detected after loading S in NC/S, while the strongest signal at g = 2.00 of S-NC indicates the effective generation of S radicals through higher temperature doping. As mentioned, high-temperature annealing seems to play a positive role in the generation of S radicals, during which the S$_8$ molecules could decompose and generate S radicals. More importantly, the NC also could stabilize the reactive radicals, which could substitute on the N-heterocyclics in NC and avoid electronic aggregation on radical through the electron-withdrawing effect of N-heterocyclic. The stabilizing effect of S-NC also could be determined by thermogravimetric analysis (TGA) in Figure 2b. The main thermogravimetric loss of S-NC is 300–400 °C, which is much higher than that of sublimed S and NC/S. The high thermal stability of S-NC also proves that most doped S is substituted on NC.

The thermal doping NC by S also could increase the interaction between absorbed S and S-NC in S-NC/S. The S-NC/S shows weak crystalline S peaks in the X-ray diffraction (XRD) profile (Figure 2c), while the XRD patterns of NC/S exhibits
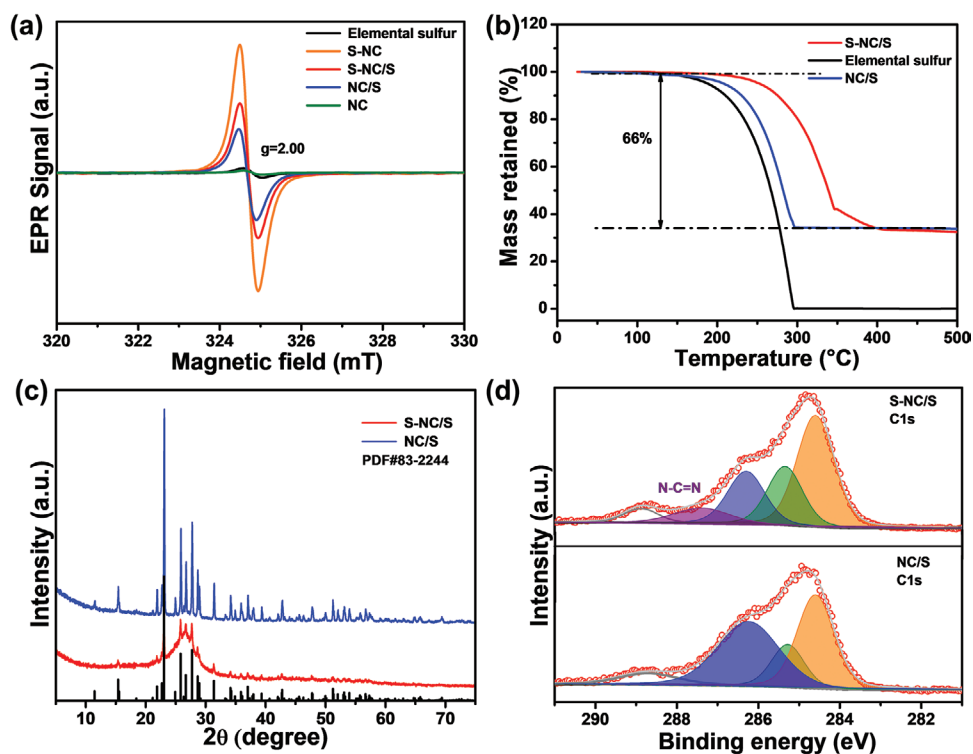

Figure 2. a) EPR curves of S-NC, S-NC/S, NC/S, NC, and elemental sulfur. b) TGA curves of the S-NC/S, elemental sulfur, and NC/S. c) XRD patterns of S-NC/S and NC/S. d) High-resolution C1s XPS spectra of S-NC/S and NC/S.

much sharper and stronger S crystal diffraction peaks, which demonstrate the increased interaction between S-NC and absorbed S. As shown in Figure S9, Supporting Information, the elemental mapping demonstrates that C, N, and S are homogenously distributed in S-NC/S. More uniform distribution and lower crystallinity of absorbed S in the S-NC/S could be attributed to the doped S in NC. Co-annealing sulfur with NC not only promotes the regulation of structure, but also generate more S radicals to capture S_8 and achieve evenly disperse.

XPS spectra in the C 1s region of S-NC/S in Figure 2d, which reveals that the C1s band can be divide into four main peaks. The peak at 285.3 eV could be identified both in the profiles of S-NC/S and NC/S, which can be assigned to the C−S bond. However, the higher intensity in S-NC/S indicated more S have been bonded onto NC/S through chemical bonding. The stronger peak of N−C=N at 287.4 eV than that in NC/S is indicated. The doped S radicals also affect the local environment after loading sublimed S. From the S2p spectra of S-NC/S and NC/S in Figure S10, Supporting Information, the S2p peaks of S-NC/S move toward higher binding energy, which indicated decrease in the electron cloud density. The introduction of S radicals could mediate the interaction between NC and loading S, so more electrons transfer from S to NC as shown in the S2p profile. Besides, the S2p 1/2 and S2p 3/2 of pre-sulfurized material (Figure 1c) disappears at low binding energy, which means the C−S single bonds are vanished due to the reaction of S radical with S_8.

As shown in **Figure 3**a, the S-NC/S of redox reactions during CV tests exhibit the lowest degree of voltage hysteresis and almost overlapped CV curves of the second and third cycles.

The curves of each cycle exhibit repeatable two main reduction peaks, which represent the typical reduction peaks of elemental sulfur to LiPSs (Li_2S_n; $4 \leq n \leq 8$) and further reduction to Li_2S_2/Li_2S.[14] The oxidation peak represents the conversion of Li_2S to elemental sulfur in Li–S batteries. From the second cycle in Figure 3a, the second reduction peak at 2.03 V and the oxidation peak at 2.40 V is slightly shifted to lower potential than that of NC/S, which suggests the reduction and oxidation become easier.[15] The current of S-NC/S is also much higher than that of NC/S (Figure S11, Supporting Information). The movement of redox peaks and higher current of S-NC/S indicates the improved polysulfide redox kinetics by the introduced S. By carefully examining the onset potential values of the Peak I, II, and III&IV, we can find that S-NC showed a remarkably lower overpotential than NC that further confirmed S-NC was more kinetically favorable for speeding up the reaction (Figure S12, Supporting Information). Meanwhile, the galvanostatic charge/discharge profiles of S-NC/S and NC/S at 0.5 C are shown in Figure S13, Supporting Information. These curves are equivalent to two discharge plateaus and one charge plateau. The discharge plateau at 2.3–2.4 V represents the formation of liquid cathode through the reduction of S_8 to soluble LiPSs, while the plateau at about 2.0 V stands for the reduction of LiPSs to insoluble low order species (Li_2S_2 and Li_2S).[16]

To operate the battery under almost quasi-equilibrium conditions, the GITT curves are measured for the 1st cycle (Figure 3b). In a typical process, a current pulse of 0.05 C was applied for 30 min to measure the closed-circuit-voltage (CCV) and then resting for 1 h to obtain the quasi-open-circuit-voltage (QOCV).[17] Compared with the NC/S, the charge/discharge
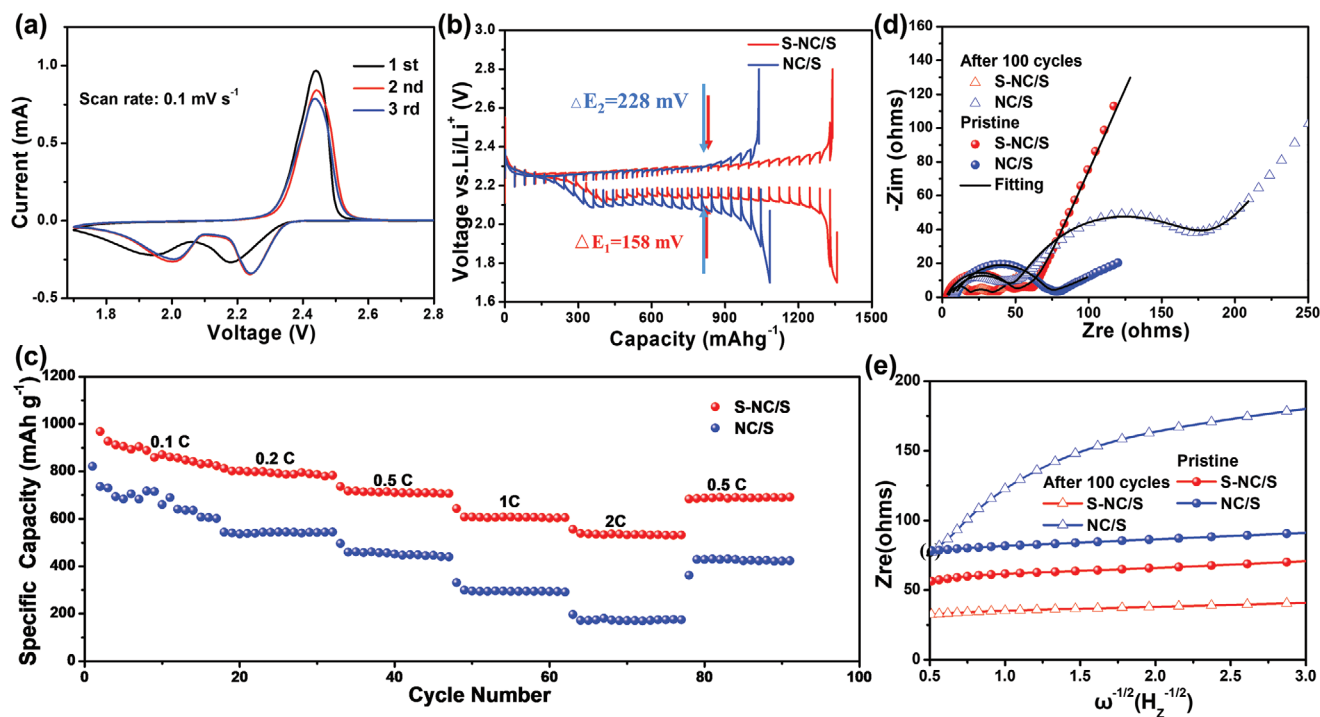

Figure 3. a) CV profiles of S-NC/S at a scan rate of 0.1 mV s^{-1}. b) GITT curves for the first charge/discharge process. c) Rate performances of S-NC/S and NC/S cathodes under various current rates. d) EIS curves. e) The relationship between Z' and $\omega^{-1/2}$ before/after cycling.

ADVANCED
SCIENCE NEWS
www.advancedsciencenews.com

NANO · MICRO
small
www.small-journal.com

plateaus of S-NC/S are longer and flatter with lower reduction voltage plateaus, and the voltage hysteresis (ΔE_1 = 158 mV) is also much lower than NC/S (228 mV) at the stages of discharge to near 800 mAh g^{-1}. Moreover, an increase of voltage hysteresis was observed as the deeper discharging NC/S battery, which is not so much significant in S-NC/S battery. The GITT data reveals that the introduced S radicals, pyridinic-N, and pyrrolic-N in NC/S could accelerate charge transfer mobility and ion transfer kinetics. The galvanostatic charge-discharge profiles of cells with S-NC/S and NC/S for the first cycle at 1C are shown in Figure S14, Supporting Information. The Li–S cell with the S-NC/S cathode shows lower polarization of 240 mV (NC/S is 355 mV), which suggests more kinetically efficiency higher compatibility with electrolyte.[18]

The rate capability of the cell with S-NC/S and NC/S cathode is examined between 1.7–2.8 V. As displayed in Figure 3c, the discharge capacities of the cell with S-NC/S at 0.1, 0.2, 0.5, and 1C after 15 cycles correspond to the value of 823.9, 783.2, 706.3, and 605.3 mAh g^{-1} respectively. Even at a higher rate of 2 C, the cell with S-NC/S electrode still presents a specific capacity of 531.9 mAh g^{-1}. When the rate reduces back to 0.5 C, a specific capacity of 691.4 mAh g^{-1} can be obtained, which was superior to other Li–S cells in the-state-of-art. The impressive rate capability of the cell with the S-NC/S electrode would be attributed to the introduced sulfur radicals during pre-vulcanization and high content of pyridinic-N and pyrrolic-N. To analyze the

S-NC on the improvement of the redox kinetics during cycling, the typical Nyquist plots of two different cathode materials at the open-circuit voltage before/after 100 cycles are measured (Figure 3d). One additional semicircle is displayed after 100 cycles, which can be attributed to the formation of another insulating layer on the lithium anode surface due to diffusion of LiPSs. The equivalent circuit models are presented in Figure S15, Supporting Information, and the result of the impedance simulation is shown in Table S2, Supporting Information. The Ohmic resistance before/after cycling of S-NC/S shows a smaller charge transfer resistance (R_{ct}) (44.37/13.60 Ω) than those of NC/S (60.98/114 Ω). More importantly, R_{sf} of the S-NC/S (13.02 Ω) after cycling is much smaller than that of the NC/S (39.1 Ω), which demonstrates that the S-NC facilitates Li-ion diffusion from the electrolyte to the electrode surface. The slope of the linear fitting plot of Z' versus $\omega^{-1/2}$ expresses the solid-state diffusion of ions inside the electrode materials, S-NC/S always maintain similar slopes in Figure 3e before and after cycling. While NC/S has a large slope after cycling. Therefore, it can be concluded that S-NC plays a very important role in preserving fast ion diffusion kinetics.[17]

In **Figure 4**a, the Li–S batteries assembled with S-NC/S cathode can retain a high discharge capacity of 931.8 mAh g^{-1} after 80 cycles with a coulombic efficiency of 99.12%, which is much higher than that of the NC/S electrode (718.7 mAh g^{-1}) after 80 cycles with a coulombic efficiency of 98.82%). Importantly,
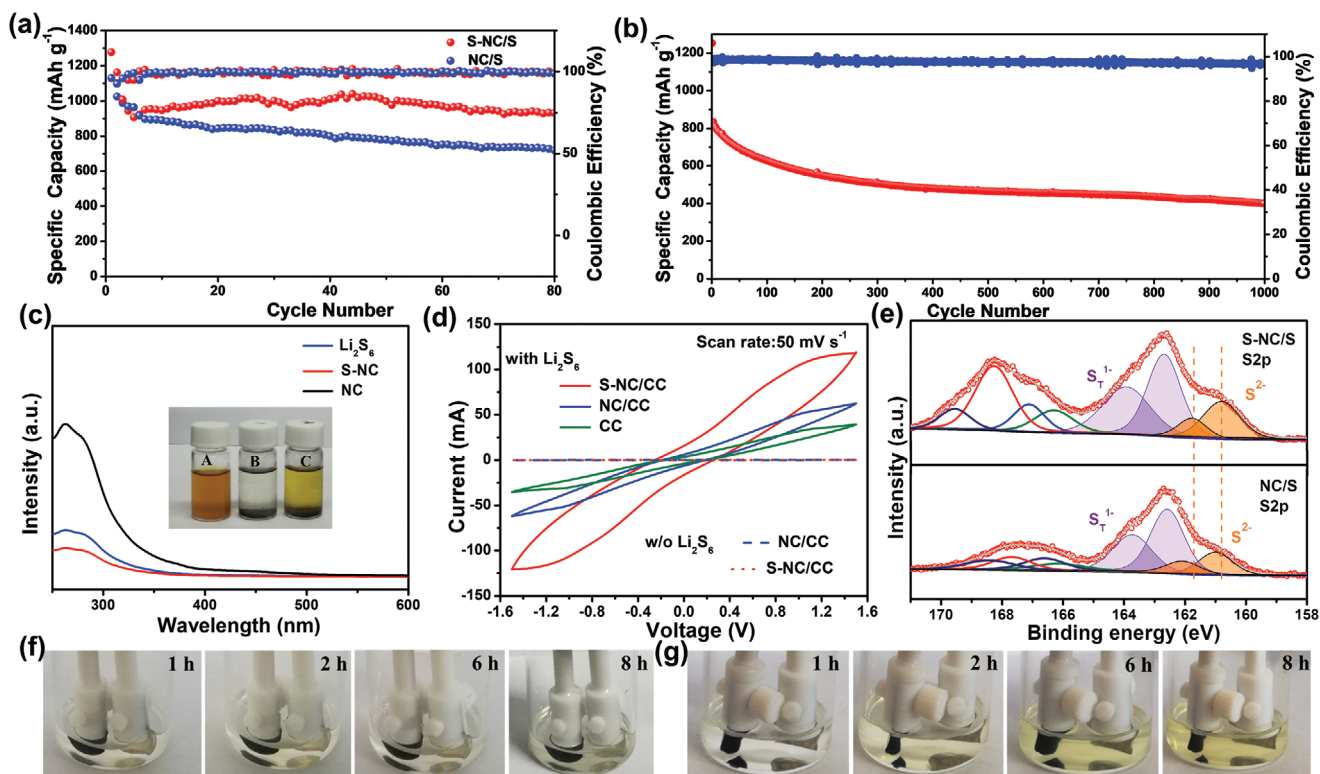

Figure 4. a) Cycling performance and Coulombic efficiency of the S-NC/S and NC/S cathodes at 0.2 C. b) The long Cycling performance and Coulombic efficiency of the S-NC/S cathode at 1 C. c) UV–vis absorption spectra of lithium polysulfide (Li$_2$S$_6$) solution before and after the addition of S-NC and NC (A represents Li$_2$S$_6$ solution, B represents S-NC, C represents NC). d) CV curve of symmetric dummy cells employing S-NC and pristine NC electrodes at a rapid scan rate of 50 mV s^{-1}. e) XPS S2p spectra S-NC/S and NC/S cathode after 100 cycles. f) Visual images of vial cells at different discharge processes by S-NC/S based Li–S battery. g) Visual images of vial cells at different discharge processes by NC/S based Li–S battery.

ADVANCED
SCIENCE NEWS
www.advancedsciencenews.com

NANO · MICRO
small
www.small-journal.com

the long-term stability of S-NC/S electrode is investigated at an even higher current density of 1 C (Figure 4b) and 399.9 mAh g^{-1} of discharge capacity is reserved after 1000 cycles, corresponding to only 0.052% of capacity decay in each cycle. The results are relatively excellent in sulfur-rich cathode materials (Table S4, Supporting Information). Figure S16, Supporting Information, shows the performances of the cells with high current density (4 C) and higher loading (0.75 mg cm^{-2} sulfur loading), respectively. The battery assembled with S-NC/S cathode shows more stability and higher capacity at 4 C current density (413 mAh g^{-1} after 100 cycles) than of NC/S (329 mAh g^{-1} after 100 cycles). It is worth mentioning that the cell of S-NC with higher loading (1.8 mg cm^{-2} sulfur loading) retains a high discharge capacity of 321.9 mAh g^{-1} after 100 cycles. The S-NC/S and NC/S cathode demonstrated outstanding electrochemical behaviors under lean electrolyte conditions at 0.5 C (Figure S17, Supporting Information) and maintained the capacity of 654 and 478 mAh g^{-1} after 100 cycles, respectively. The excellent durability of S-NC/S in Li–S battery is attributed to the doped nitrogen and the introduction of sulfur radicals, which could effectively inhibit the shuttle effect of polysulfide lithium and beneficial to well-localized active materials within the cathode side. To verify the stabilizing ability on LiPSs, the S-NC was mixed with Li$_2$S$_6$ solution, which became clear in 12 h. But, the solution with NC still displayed a yellow color after 12 h (Figure S18, Supporting Information). In the UV–vis spectroscopy (Figure 4c), UV-absorbing peaks of Li$_2$S$_6$ in solution also decreased significantly after the addition of S-NC.

The kinetics of redox reactions was systemically probed by CV measurement using symmetric dummy cells with S-NC in both electrodes and Li$_2$S$_6$ solution as electrolyte (Figure 4d).[19] The S-NC exhibited a higher current density than that of NC, implying the significantly enhanced redox kinetics between liquid-phase polysulfides. The CV curves at different scan rates were also carried out to further illuminate the electrical redox on the interface of S-NC (Figure S19, Supporting Information). In this case, the CV of S-NC still has a large current at 1000 mV s^{-1}, which significantly enhances reaction kinetic

during the conversion of polysulfides. The introduced sulfur radicals in S-NC could provide abundant triple-phase interfaces with the collaboration of chemisorption, polysulfides. As a result, the conversion from Li$_2$S$_2$ to Li$_2$S is improved to achieve higher sulfur utilization. The high electron transferability was also further proved by EIS due to the excellent compatibility on S-NC interface and high conductivity after S doping (Figure S20, Supporting Information).

The S2p XPS spectra of S-NC/S and NC/S cathode after 100 cycles is exhibited in Figure 4e. The peaks located at 166–169 eV belonged to sulfite and sulfate, which would be the product of oxidized sulfur species during SEI formation.[20] The peaks at 161.0–162 eV assigning to S^{2-} in Li$_2$S, and the peaks at 162.5 and 163.7 eV assigning to bridging sulfur terminal sulfur (S$_T^1$) belongs to Li$_2$S$_2$.[21] Moreover, the peak of Li$_2$S in S-NC/S moves to lower binding energy at 160.8 eV than that in NC/S, which indicates more Li$_2$S is produced due to the introduced S radical. Figure S21, Supporting Information, displays the high-resolution spectrums of the Li 1s and N 1s. The bond of Li−N and Li−S can be observed in both S-NC/S and NC/S. Figure S22, Supporting Information, shows visible images of cycled separators and lithium anodes with S-NC/S and NC/S cathode after 100 cycles respectively. The black deposition of Li$_2$S/Li$_2$S$_2$ could not be identified on lithium anode with S-NC/S cathode, which is likely attributed to the accelerated conversion of LiPSs on S-NC cathode to eliminate the shuttling effect and result in greatly improved durability. Figure 4f,g shows photographs of transparent vial cells. After 8 h, the transparent electrolyte changes to yellowish in the NC/S owing to the gradually dissolved LiPSs. However, the electrolyte in the S-NC/S remained transparent, which also could further imply the high active surface of the S-NC to prevent the dissolution of LiPSs.

To better understand S reduction pathways of both S-NC and NC, the density functional theory (DFT) calculations (**Figure 5**a–e) were performed to evaluate the reversible formation of Li$_2$S from S$_8$ and Li, and how the binding strength of the Li–S end of linear lithium polysulfides (Li$_2$S$_2$) is influenced
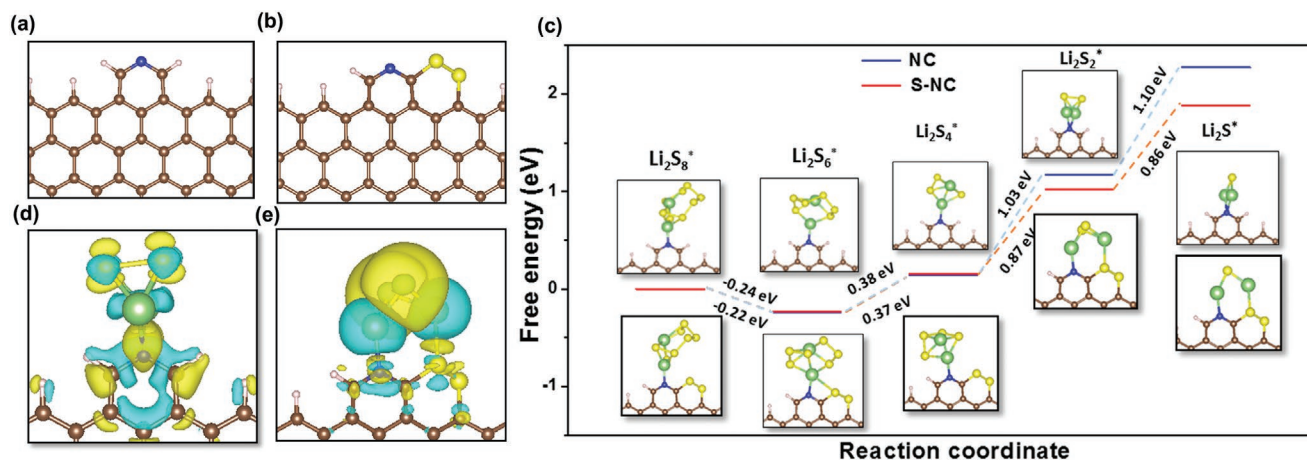

Figure 5. Energy profiles for Li sulfides S-NC and NC. Structures of NC (a) and S-NC (b) used in first-principles calculations. c) Energy profiles for the reduction of LiPSs on substrates. (insets) The optimized adsorption conformations of intermediate species on S-NC and NC substrate. Charge density difference isosurfaces for the reduction of Li$_2$S$_2$ on a substrate of NC (d) and S-NC (e) at front-view. The blue and yellow indicate the regions of charge gain and loss (of ±0.001 e per bohr^3), respectively. Brown, white, blue, yellow, and green balls represent C, H, N, S, and Li atoms, respectively.

by introducing S atoms into the graphene lattice.[22] Figure 5c shows the optimized structures of the intermediates and their Gibbs free energy profiles. The steps for the double reduction of S_8 with Li^+ to form Li_2S_8, after a series of reduction and disproportionation processes, forming the intermediates of Li_2S_6, Li_2S_4, and Li_2S_2, leads to the end product of Li_2S. The Gibbs free energies were calculated for the above reactions on both S-NC and NC substrates. The formation of Li_2S from Li_2S_2 has the largest positive Gibbs free energy, indicating that this is the rate-limiting step in the whole discharge process. Compared with the case of NC (1.10 eV), the Gibbs free energy decreased to 0.86 eV by introducing the sulfur atom of S-NC. The lower Gibbs free energy on S-NC for the reduction of Li_2S_2 indicates that the reduction of S is thermodynamically more favorable on S-NC than on NC substrate, which could largely contribute to the improving battery performance. Moreover, the charge density difference isosurfaces of Li_2S_2 on the substrate of NC (Figure 5d) and S-NC (Figure 5e) at front-view. The blue and yellow colors indicate the regions of charge gain and loss (of ±0.001 e per bohr³), respectively. Compared with the case of NC, the blue region near the S−S bond increases, and yellow areas of Li also increases on the S-NC simulation optimizations structure, and electron-rich regions are more conducive to the break of S−S bond, which further declares that the reduction of Li_2S_2 is more opportune on S-NC than on NC substrate. The finding is consistent with characterization analysis as shown in XPS spectra (Figure 4e).

Besides, the adsorption energies of Li_2S_n (n = 1, 2, 4, 6, 8) clusters on the S-NC surface are displayed in Figure S23, Supporting Information. Encouragingly, compared to NC, the value of E_{ads} on S-NC significantly increased, corresponding to 4.02, 4.61, 7.13, 5.76, and 4.44 eV, respectively. Especially, the strong adsorption energies of the Li_2S_4 cluster, representing a significant force between S-NC and soluble polysulfide. The structure of S-NC can improve the adsorption strength of the Li_2S_n cluster and provide active sites for the attraction of the Li atom. According to our calculations, our DFT consequences demonstrate that the coexistence of N and S regarding the synergistic effect clearly, and can significantly enhance the conversion of lithium polysulfides, which support our experimental observations.

3. Conclusion

In summary, the S doped NC has been prepared by copolymerization from DAMN and elemental sulfur. Due to the poor thermal stability of amino groups on DAMN, large quality of S radicals is substituted on the neighbor of C=N. With the unique structure, the S-NC significantly enhances reaction kinetics of polysulfides conversion to inhibit polysulfide shuttle in the battery. Moreover, the energy barriers during ions transfer also decreased, which lead to smaller polarization potential and improved rate performance. Therefore, the presence of sulfur radical on the neighbor of C=N in S-NC could effectively lower Gibbs free energy during the reduction of Li_2S_2. This work would open the highway for the design and fabrication of metal-free cathode for Li–S batteries.

4. Experimental Section

Materials Synthesis: The NC doped by richening sulfur (S-NC) has been synthesized by thermal polymerization of DAMN (5.4 g) in melted sulfur (3.5 g) at 400 °C for 12 h with nitrogen protection, and then soxhlet was extracted by toluene to dissolve excess sulfur. As a control sample, NC was synthesized via the same method without the addition of sulfur during thermal polymerization. Then, the obtained product and sublimed sulfur were uniformly grounded and vacuumed in a sealed glass tube and heated at 155 °C for 12 h, and then raised to 200 °C for 30 min to remove the sulfur on the surface. After cooling to room temperature, the composites, namely S-NC/S and NC/S, were obtained (corresponding to S-NC and NC as a precursor, respectively).

Material Characterization: The structures and morphologies of obtained composites were characterized by XRD (X'Pert PRO MPD, Holland), field emission scanning electron microscopy (FE-SEM) (Hitachi S-4800, Japan). Raman analysis was performed on Jobin Yvon HR800 Raman spectrometer. The functional groups in the samples were studied by XPS (Thermo Scientific ESCALab250Xi). EPR spectra were recorded using a Bruker EMX spectrometer (X band) at 77 K. The TGA was determined by TG/DTA 6300 system at a heating rate of 10 °C min⁻¹. UV–vis spectroscopy was executed by UV-2700, Shimadzu.

Electrochemical Measurements: The electrochemical measurements were conducted using LIR2032 coin cells with pure Li foil as the counter. Cathode electrodes consist of sublimed sulfur, carbon black, and polyvinylidene difluoride in a weight ratio of 7:2:1 in N-methyl-2-pyrrolidinone. The slurry was coated onto a current collector made from aluminum foil and then was dried under vacuum at 60 °C for 12 h. The electrodes were cut to disks, typically with a diameter of 12 mm, and the average mass of the sulfur loading within the coin cells was around 0.7–1.0 mg cm⁻². The amount of electrolyte in the assembled battery is 25 μL per cell, and the material under lean electrolyte conditions with 15 μL per cell. The cell assembly was carried out in an Ar-filled glovebox with the concentration of moisture and oxygen below 0.1 ppm. The separator was microporous polypropylene and the organic electrolyte was composed of 1.0 M LiTFSI in 1,2-dimethoxyethane and 1,3-dioxolane (DME/DOL, 1:1 vol) with 1.0% $LiNO_3$ (analytical grade). The galvanostatic discharge-charge cycle tests and rate tests were carried out on a Land Battery Measurement System (Land CT2001A, China) at various current densities of 0.1–2 C (1 C = 1675 mA g⁻¹) in the voltage range of 1.7–2.8 V versus Li/Li⁺ at room temperature. The specific capacity was calculated based on the mass of sulfur. Cyclic voltammetry (CV) curves were conducted using an Ametek PARSTAT4000 electrochemistry workstation between 1.7 and 2.8 V at a scan rate of 0.1 mV s⁻¹. Electrochemical impedance spectroscopy (EIS) tests were also performed using Ametek PARSTAT4000 electrochemistry workstation in the frequency range of 100 kHz to 10 MHz with AC voltage amplitude of 10 mV.

Adsorption Experiment: Sublimed S and Li_2S in a molar ratio of 5:1 were added into 1,2-dimethoxyethane and 1,3-dioxolane (DME/DOL, 1:1 vol) at the same time, then aged at 55 °C for 12 h under stirring, and homogeneous 5 mM Li_2S_6 solution was obtained. The operations were carried out in an Ar-filled glovebox with the concentration of moisture and oxygen below 0.1 ppm. The adsorption ability of S-NC and NC composites was tested using a UV-2700 spectrophotometer (Shimadzu).

Fabrication of Li_2S_6 Symmetric Cells and Kinetic Study: The electrodes of symmetric cells were fabricated without the presence of elemental sulfur. Host materials and PVDF binder were mixed into the NMP with a weight ratio of 4:1 and then coated onto the electrodes. Here carbon cloth was used as the identical working and counter electrodes. 60 μL catholyte (0.5 M Li_2S_6 and 1 mol L⁻¹ LiTFSI dissolved in DOL/DME (v/v = 1/1)) was added into each coin cell. CV and EIS tests were carried out on the Ametek PARSTAT4000 electrochemistry workstation. CV was performed at a scan rate of 50 mV s⁻¹ in the voltage range of −1.5 ≈1.5 V, and (EIS) measurement was performed at open-circuit voltage with a frequency range from 0.01 to 10⁵ Hz.[23]

Theoretical Calculation: All calculations were performed using the DFT method implemented in the Vienna ab initio simulation package (VASP).[24] The projector augmented wave (PAW) method was used to

describe electron-ion interactions.[25] The gradient-corrected Perdew-Burke-Ernzerh (GGA-PBE) functional was adopted to describe electron exchange and correlation energy.[26] The edge of graphene containing 5×1 unit cells was used to model S-NC and NC systems, and model N and S dopant atoms at graphene edges. The cutoff energy for the plane-wave basis set was set as 500 eV, and the total energy convergence was set to be lower than 1×10^{-6} eV, with the force convergence set at 0.01 eV Å^{-1} for geometric optimization. The first Brillouin zone was sampled with $3 \times 1 \times 1$ and $5 \times 5 \times 1$ Monkhorst Pack mesh of k points was used for the Brillouin zone integration. The DFT-D3 empirical correction method was employed to describe van der Waals interactions.[27]

The calculation formulas are as follows:[28]

$$\Delta G = G\left(Li_2S_{n-2}^*\right) + G\left(Li_2S\right) - G\left(Li_2S_n^*\right) - 4G\left(Li^+ + e^-\right) \tag{1}$$

The adsorption energies of Li_2S_n ($n = 1, 2, 4, 6, 8$) clusters on the S-NC surface are calculated using the following formula:[29]

$$E_{ads} = E\left(substrate\right) + E\left(Li_2S_n\right) - E\left(substrate/Li_2S_n\right) \tag{2}$$

where E (substrate) is the energy of S-NC or NC, E (Li_2S_n) is the energy of the Li_2S_n cluster, and E (substrate/Li_2S_n) is the energy of S-NC or NC with Li_2S_n adsorption. Here, a positive E_{ads} means attractive interaction.

The ppm value represents the difference of chemical shift between two different carbon assignments and NMR characterizations were used to evaluate the shielding effect originated from the electron cloud surrounded targeting nuclei. Herein, the calculated chemical shift was presented, and compared with the experimental solid-state NMR characterizations. All of these section calculations were performed with a plane wave-based DFT implementation within Gaussian by a base set of 6-31G*. The B3LYP density functional used in this study has been demonstrated to be accurate enough for NMR simulation of NC and S-NC. There is a commonly used approach for converting shielding constants into chemical shifts. Chemical shifts were obtained by subtracting calculated shielding constants from the value of TMS B3LYP/6-31G* GIAO.

Supporting Information

Supporting Information is available from the Wiley Online Library or from the author.

Acknowledgements

Conflict of Interest

The authors declare no conflict of interest.

Keywords

[1] a) L. Li, G. Ruan, Z. Peng, Y. Yang, H. Fei, A. R. Raji, E. L. Samuel, J. M. Tour, *ACS Appl. Mater. Interfaces* **2014**, *6*, 15033; b) Y. Qiu, W. Li, W. Zhao, G. Li, Y. Hou, M. Liu, L. Zhou, F. Ye, H. Li, Z. Wei, *Nano Lett.* **2014**, *14*, 4821; c) Z. Guangmin, P. Songfeng, L. Lu, W. Da-Wei, W. Shaogang, H. Kun, Y. Li-Chang, L. Feng, C. Hui-Ming, *Adv. Mater.* **2014**, *26*, 625;. d) X. Yang, L. Zhang, F. Zhang, Y. Huang, Y. Chen, *ACS Nano* **2014**, *8*, 5208; e) L. Zhang, F. Wan, X. Wang, H. Cao, X. Dai, Z. Niu, *ACS Appl. Mater. Interfaces* **2018**, *10*, 5594.

[2] D.-Y. Wang, W. Guo, Y. Fu, *Acc. Chem. Res.* **2019**, *52*, 2290.

[3] T. Sun, J. Xie, W. Guo, D.-S. Li, Q. Zhang, *Adv. Energy Mater.* **2020**, *10*, 1904199.

[4] X. Ding, J. Guo, X. Feng, Y. Honsho, J. Guo, S. Seki, P. Maitarad, A. Saeki, S. Nagase, D. Jiang, *Angew. Chem., Int. Ed. Engl.* **2011**, *50*, 1289.

[5] W. Wang, Z. Cao, G. A. Elia, Y. Wu, W. Wahyudi, E. Abou-Hamad, A.-H. Emwas, L. Cavallo, L.-J. Li, J. Ming, *ACS Energy Lett.* **2018**, *3*, 2899.

[6] a) K. Pierre, A. Markus, T. Arne, *Angew. Chem., Int. Ed.* **2010**, *47*, 3450; b) S. H. Je, H. J. Kim, J. Kim, J. W. Choi, A. Coskun, *Adv. Funct. Mater.* **2017**, *27*, 1703947; c) S. N. Talapaneni, T. H. Hwang, S. H. Je, O. Buyukcakir, J. W. Choi, A. Coskun, *Angew. Chem., Int. Ed.* **2016**, *55*, 3106.

[7] S. N. Talapaneni, T. H. Hwang, S. H. Je, O. Buyukcakir, J. W. Choi, A. Coskun, *Angew. Chem., Int. Ed.* **2016**, *128*, 3158.

[8] a) Z.-Q. Jin, Y.-G. Liu, W.-K. Wang, A.-B. Wang, B.-W. Hu, M. Shen, T. Gao, P.-C. Zhao, Y.-S. Yang, *Energy Storage Mater.* **2018**, *14*, 272; b) J. Fanous, M. Wegner, J. Grimminger, Ä. Andresen, M. R. Buchmeiser, *Chem. Mater.* **2011**, *23*, 5024.

[9] J. Song, T. Xu, M. L. Gordin, P. Zhu, D. Lv, Y.-B. Jiang, Y. Chen, Y. Duan, D. Wang, *Adv. Funct. Mater.* **2014**, *24*, 1243.

[10] Y. Wang, L. Xu, M. Wang, W. Pang, X. Ge, *Macromolecules* **2014**, *47*, 3901.

[11] a) L. Xiao, Y. Cao, J. Xiao, B. Schwenzer, M. H. Engelhard, L. V. Saraf, Z. Nie, G. J. Exarhos, J. Liu, *Adv. Mater.* **2012**, *24*, 1176; b) H. Chen, C. Wang, C. Hu, J. Zhang, S. Gao, W. Lu, L. Chen, *J. Mater. Chem. A* **2015**, *3*, 1392.

[12] H. Yuan, W. Zhang, J.-g. Wang, G. Zhou, Z. Zhuang, J. Luo, H. Huang, Y. Gan, C. Liang, Y. Xia, J. Zhang, X. Tao, *Energy Storage Mater.* **2018**, *10*, 1.

[13] a) L. Cai, J. He, Q. Liu, T. Yao, L. Chen, W. Yan, F. Hu, Y. Jiang, Y. Zhao, T. Hu, Z. Sun, S. Wei, *J. Am. Chem. Soc.* **2015**, *137*, 2622; b) R. Steudel, T. Chivers, *Chem. Soc. Rev.* **2019**, *48*, 3279.

[14] a) H. Wang, Y. Yang, Y. Liang, J. T. Robinson, Y. Li, A. Jackson, Y. Cui, H. Dai, *Nano Lett.* **2011**, *11*, 2644; b) S. Chen, B. Sun, X. Xie, A. K. Mondal, X. Huang, G. Wang, *Nano Energy* **2015**, *16*, 268.

[15] J. Yoo, S. J. Cho, G. Y. Jung, S. H. Kim, K. H. Choi, J. H. Kim, C. K. Lee, S. K. Kwak, S. Y. Lee, *Nano Lett.* **2016**, *16*, 3292.

[16] H. Lin, L. Yang, X. Jiang, G. Li, T. Zhang, Q. Yao, G. W. Zheng, J. Y. Lee, *Energy Environ. Sci.* **2017**, *10*, 1476.

[17] S. Wang, J. Liao, X. Yang, J. Liang, Q. Sun, J. Liang, F. Zhao, A. Koo, F. Kong, Y. Yao, X. Gao, M. Wu, S.-Z. Yang, R. Li, X. Sun, *Nano Energy* **2019**, *57*, 230.

[18] a) F. Pei, L. L. Lin, D. H. Ou, Z. M. Zheng, S. G. Mo, X. L. Fang, N. F. Zheng, *Nat. Commun.* **2017**, *8*, 482; b) P. Y. Zhai, J. Q. Huang, L. Zhu, J. L. Shi, W. C. Zhu, Q. Zhang, *Carbon* **2017**, *111*, 493.

[19] a) Y. Wang, R. Zhang, J. Chen, H. Wu, S. Lu, K. Wang, H. Li, C. J. Harris, K. Xi, R. V. Kumar, S. Ding, *Adv. Energy Mater.* **2019**, *9*, 1900953; b) Z. Yuan, H. J. Peng, T. Z. Hou, J. Q. Huang, C. M. Chen, D. W. Wang, X. B. Cheng, F. Wei, Q. Zhang, *Nano Lett.* **2016**, *16*, 519.

[20] a) S. Wei, L. Ma, K. E. Hendrickson, Z. Tu, L. A. Archer, *J. Am. Chem. Soc.* **2015**, *137*, 12143; b) C. P. Yang, Y. X. Yin, Y. G. Guo, L. J. Wan, *J. Am. Chem. Soc.* **2015**, *137*, 2215; c) K. E. Hendrickson, L. Ma, G. Cohn, Y. Lu, L. A. Archer, *Adv. Sci.* **2015**, *2*, 1500068.

[21] M. I. Nandasiri, L. E. Camacho-Forero, A. M. Schwarz, V. Shutthanandan, S. Thevuthasan, P. B. Balbuena, K. T. Mueller, V. Murugesan, *Chem. Mater.* **2017**, *29*, 4728.

[22] a) Z. Du, X. Chen, W. Hu, C. Chuang, S. Xie, A. Hu, W. Yan, X. Kong, X. Wu, H. Ji, L. J. Wan, *J. Am. Chem. Soc.* **2019**, *141*, 3977; b) R. S. Assary, L. A. Curtiss, J. S. Moore, *J. Phys. Chem. C* **2014**, *118*, 11545.

[23] a) J. Xu, W. Zhang, H. Fan, F. Cheng, D. Su, G. Wang, *Nano Energy* **2018**, *51*, 73; b) H. Yuan, H.-J. Peng, B.-Q. Li, J. Xie, L. Kong, M. Zhao, X. Chen, J.-Q. Huang, Q. Zhang, *Adv. Energy Mater.* **2019**, *9*, 1802768; c) X. Yang, X. Gao, Q. Sun, S. P. Jand, Y. Yu, Y. Zhao,

X. Li, K. Adair, L. Y. Kuo, J. Rohrer, J. Liang, X. Lin, M. N. Banis, Y. Hu, H. Zhang, X. Li, R. Li, H. Zhang, P. Kaghazchi, T. K. Sham, X. Sun, *Adv. Mater.* **2019**, *31*, 1901220.

[24] G. Kresse, J. Furthmüller, *Comput. Mater. Sci.* **1996**, *6*, 15.

[25] P. E. Blöchl, *Phys. Rev. B* **1994**, *50*, 17953.

[26] J. P. Perdew, K. Burke, M. Ernzerhof, *Phys. Rev. Lett.* **1996**, *77*, 3865.

[27] Q. Wu, W. Yang, *J. Chem. Phys.* **2002**, *116*, 515.

[28] G. Zhou, S. Zhao, T. Wang, S.-Z. Yang, B. Johannessen, H. Chen, C. Liu, Y. Ye, Y. Wu, Y. Peng, C. Liu, S. P. Jiang, Q. Zhang, Y. Cui, *Nano Lett.* **2020**, *20*, 1252.

[29] F. Li, Y. Su, J. Zhao, *Phys. Chem. Chem. Phys.* **2016**, *18*, 25241.

2004631 (9 of 9)